Reconstruction of HPGe Detector Modeling for Efficiency Calibration

Zhang Changfan*, Hu Guangchun, Zeng Jun, Xiang Qingpei, Gong Jian

China Academy of Engineering Physics, Institute of Nuclear Physics and Chemistry, Mianyang city 621900, China

High purity germanium (HPGe) detector is a prior choice for determining the activity of the radioactive samples for nuclear diagnostics of Inertial Confinement Fusion (ICF) experiments. Efficiency calibration of gamma rays at a close distance from the surface of an HPGe detector is a crucial issue. So far as the detector structure is precisely clarified, a model of the detector can be well developed, based on which Gamma-ray detection efficiencies can be calculated accurately using Monte Carlo method. In this paper, internal geometry and structure except for dead layers of the HPGe detector is obtained by X-ray radiography and 3D reconstruction. The optimal dead layers of the germanium crystal are determined by tracing the minimal sum squared residual (SSR) of gamma-ray efficiencies between calculations and measurements for standard planar sources.

Keywords HPGe detector, Efficiency calibration, MC modeling, Nuclear diagnostics

1. Introduction

Nuclear diagnostics of inertial confinement fusion (ICF) experiments are critical to achieve ignition at a facility such as National Ignition Facility and Shenguang-III Laser Facility [1–4]. A key nuclear diagnostic is the detection of radiochemical samples following implosions [5–9]. The radiochemical samples can provide quantitative data on capsule performance parameters such as fuel areal density, neutron yield, neutron energy spectral information and so on [10–13]. The radiochemical samples, i.e. diagnostic indicators, come from materials which originally either present naturally in the capsule or doped specifically into the capsule. Iridium and Scandium are such essential indicators specifically doped into the capsule to diagnose ignition failures on National Ignition Campaign targets [14–15]. Reactions of ^{191}Ir(n,2n)^{190}Ir, ^{191}Ir(n,3n)^{189}Ir, ^{45}Sc(n,2n)^{44}Sc, and ^{45}Sc(n,2n)^{43}Sc provide radiochemical signatures over the high regime of incident neutron energy. The activity of the radioactive products can be determined by emitted gamma rays. However, this capability is limited by the amounts of the isotopes loaded inside the capsule without affecting performance and the collection efficiency of the capsule debris after implosion. High purity germanium (HPGe) detector is a prior choice for determining the activity of these radioactive samples because of its superior energy resolution. Anyway, the efficiency is quite limited for gamma-ray detection of HPGe detector compared with other kinds of detectors. Decreasing the distance between detector window and radioactive source is helpful to solve the dilemma. Therefore, efficiency calibration of gamma rays at a very close distance from the surface of an HPGe detector is a crucial issue. Considering the problem of the coincidence at a close distance, it is very important to construct a precise model of the HPGe detector. Therefore, gamma-ray efficiencies can be calculated accurately at an arbitrary distance from the surface of an HPGe detector using Monte Carlo method as long as the detector model is confirmed.

In recent years, radiography technologies such as CT scan or collimated gamma-ray scan are employed to reconstruct a very precise model for HPGe detectors [16–20]. Dead layers of the germanium crystal are also determined by standard radioactive sources [21,22].

In this paper, we focus on the precise modeling of an HPGe detector for efficiency calibration for the further diagnostics of ICF. Internal geometry and structure except for dead

layers of the HPGe detector is obtained by X-ray radiography and 3D reconstruction. Several planar sources are utilized to calibrate the efficiencies at a certain distance from the surface of the HPGe detector window. Dead layers of the germanium crystal are determined by tracing the minimal sum squared residual of gamma-ray efficiencies between the calculations and the measurements. Nonuniform distribution of the dead layer is supposed and the corresponding model improves the accuracy of the calculated efficiencies.

2. Experiment and Methods

2.1 Apparatus

An HPGe detector is utilized to calibrate the efficiency. The detector is installed in a shielding chamber of lead. The nominal relative efficiency of this detector is 40% compared to a 3 inch × 3 inch NaI (Tl) crystal as measured at 1333 keV. The resolution of the detector is 1.88keV @ 1332keV of the ^{60}Co gamma-ray energy. The detector is connected to a Digi-multichannel analyzer, in which the pre-amplifier is integrated. The high voltage is set to positive 3050V and the rise-time is 8.00 μs. The course gain and fine gain are set as 20 and 1.18, respectively. Spectra are recorded over 16384 channels up to the energy level of 2 MeV. A Canberra Genie 2000 software (Version3.1.4) is used to acquire gamma-ray spectra.

2.2 Standard source

Several standard planar sources ^{241}Am, ^{60}Co, ^{133}Ba, ^{152}Eu and ^{166}Ho are utilized for the efficiency calibration. The sources are titrations of the radioactive solution on the filter paper, sealing within a PMMA container each. The radius of each filter paper is 18 mm. The uncertainty of the activity for each source is certified 2%.

2.3 Measurement

Each standard source is placed on a PMMA bracket which is set on the detector. The distance between the source and the detector window is 9.20 cm. The measurement layout is illustrated in Fig. 1.

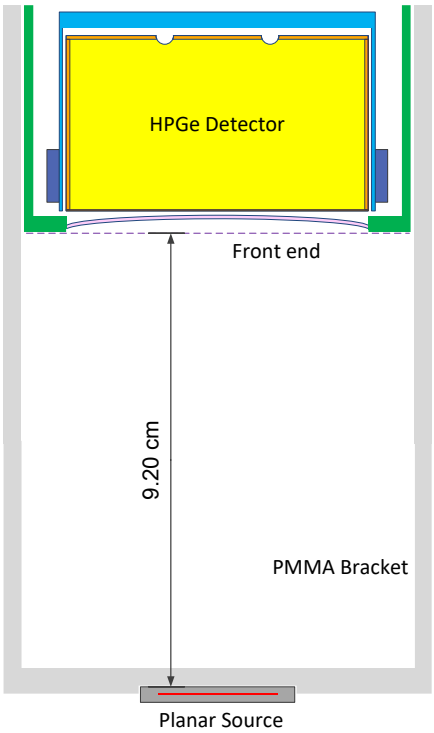

Fig. 1. Efficiency calibration for the planar sources at the distance of 9.20 cm between the source and the detector window.

The counting dead time ranges from 0.2% to 6.2%, depending on the activity of the source, which is consequently corrected during counting. The acquisition time, corresponding to at least 10^5 counts in the full energy peak, is sufficient to assure good counting statistics. The energy ranges from 59 keV to 1408 keV. The efficiency of the full energy peak $\varepsilon(E_i)$ is calculated by the following function:

$$\varepsilon(E_i) = \frac{S(E_i)}{A\eta(E_i)t_{live}}.$$

Here $S(E_i)$ is the full energy peak area of the peak E_i, A is the activity of the standard source, $\eta(E_i)$ is the intensity of the peak E_i, t_{live} is the live time of the measurement.

The measured efficiencies for gamma rays at a distance of 9.20 cm from the detector window is shown in Fig. 2.

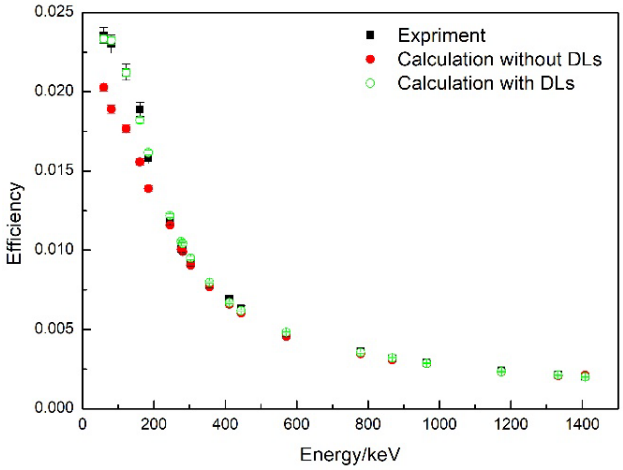

Fig. 2. The measured efficiencies (black squares) and calculated efficiencies (red circles and green hollow circles) for gamma rays at a distance of 9.20 cm from the detector window.

2.4 Radiography for MC modeling

Even though dimension of the detector is always provided by the manufacturer (not the case for this HPGe detector), the discrepancies between the nominal values and the actual values always exist. To obtain a reliable model, X-ray radiography and 3-D reconstruction illustrated in Fig. 3 were performed to determine the detector's precise dimensions. The geometrical structure and corresponding parameters of the detector, listed in Table1 and displayed in Fig. 3, are used for MC modeling.

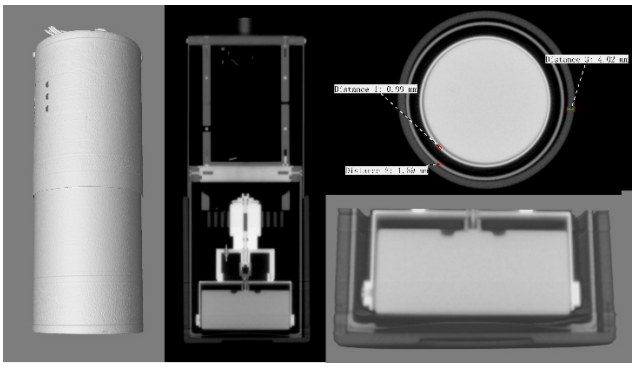

Fig. 3. X-ray radiography and the 3-D reconstruct of the detector.

Table 1 Parameters of the HPGe detector

Structure	Material	Density/g/cm^3
Crystal	high purity germanium	5.32
Beryllium window	beryllium	1.85
Inner lateral cap	copper	8.96
Fastening belt	copper	8.96
External lateral cap	aluminum	2.70

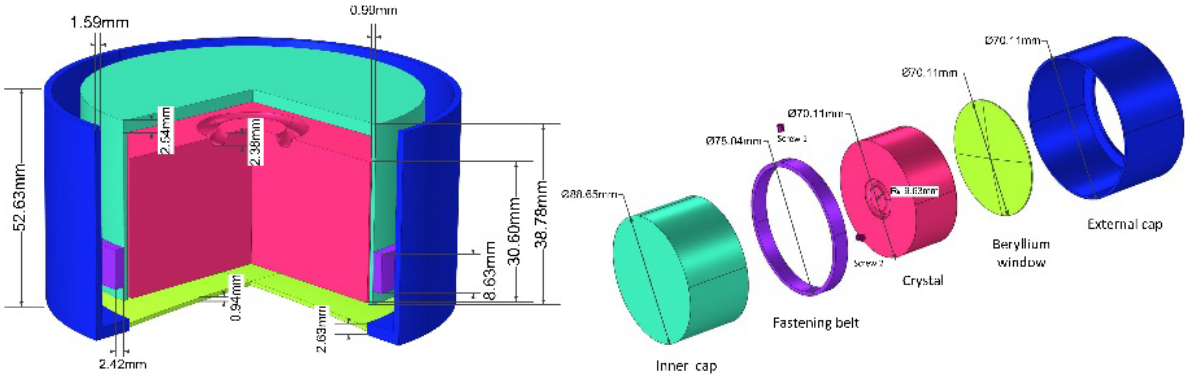

Fig. 4. Geometry parameters of the HPGe detector.

In the radiography, several geometrical subtle details are revealed. For instance, there is a circinate groove on the rear of the germanium crystal, the beryllium window is not flat, and the PMMA bracket is not homocentric with the crystal. All these details mentioned above, in Fig. 5, are considered in model reconstruction. However, it is worthy to note that the crystal dead layer (DL) thickness cannot be obtained by X-ray radiography. Determination for the DL thickness will be discussed in the latter section.

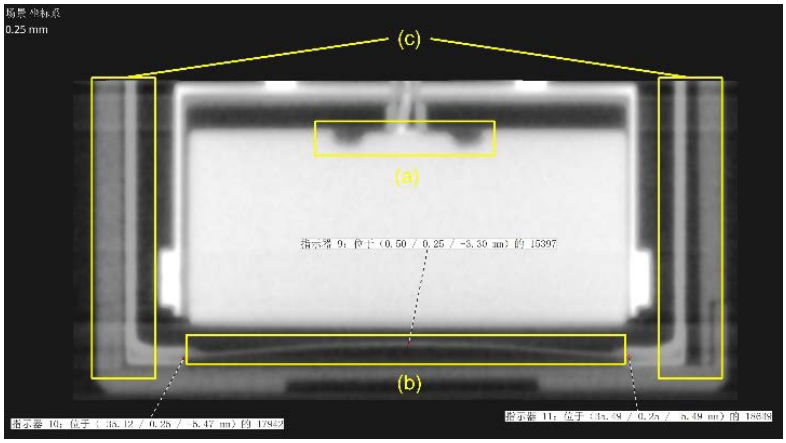

Fig. 5. Geometric subtle details are revealed in the X-ray radiography, such as (a) a groove on the rear crystal, (b) curving beryllium window, and (c) non-central symmetric PMMA bracket.

The gamma-ray measurement model, which contains the HPGe detector, the PMMA bracket and the standard source, was constructed by MCNP5 code [21]. The calculated efficiencies without DLs are shown as red dots in Fig. 2. The relative deviations between calculated efficiencies without DLs and measured ones are shown in Fig. 6(a). The results indicate that dead layers are needed to be considered.

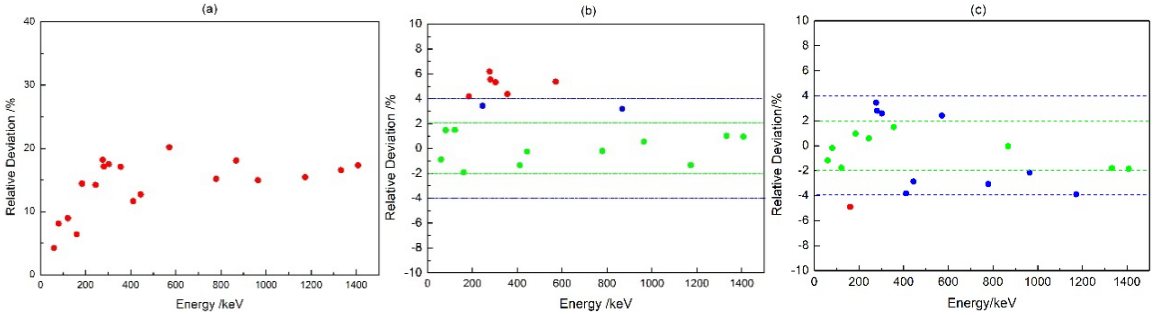

Fig. 6. Deviation of gamma-ray efficiencies between experiments and calculations (a) without DLs (b) with DLs and (c) with corrected DLs.

2.5 Determination for thicknesses of DLs

Here sum squared residual (SSR) of gamma-ray efficiencies is employed to calculate the optimal thicknesses of DLs:

$$SSR = \sum_{Ei<200keV} (\varepsilon_{cal,Ei} - \varepsilon_{\exp,Ei})^2 ,$$

where $\varepsilon_{cal,Ei}$ and $\varepsilon_{\exp,Ei}$ are the calculated efficiency and the measured efficiency at the energy E_i, respectively. The optimal DLs will minimize the SSR of gamma-ray efficiencies.

Because low-energy gamma rays are hard to penetrate the crystal and the efficiencies of them are sensitive to the thicknesses of the front-end and lateral DLs. Determination for the thicknesses of front-end and lateral DLs of the crystal can take advantage of the low-energy gamma rays. Likewise, determination for the thickness of the back-end DL can take advantage of high-energy gamma rays.

Determination for the optimal thicknesses of front-end and lateral DLs relies on 59 keV @ ^{241}Am, 81 keV @ ^{166}Ho, 121 keV@^{152}Eu and 160 keV@^{133}Ba. The *SSR* contour of low-energy gamma-ray efficiencies at different thicknesses of front-end and lateral DLs are shown in Fig. 7. Here the initial thicknesses of front-end and the lateral DLs are set as 0.001 cm and 0.04 cm, respectively. And the steps of front-end and the lateral DLs are set as 0.001 cm and 0.01 cm, respectively. Specially, the front-end DL is also set as 0.00001 cm and relevant calculations are shown in Fig. 7. The corresponding abscissa for the front-end Dl of 0.00001 cm is labeled as 0.000 cm.

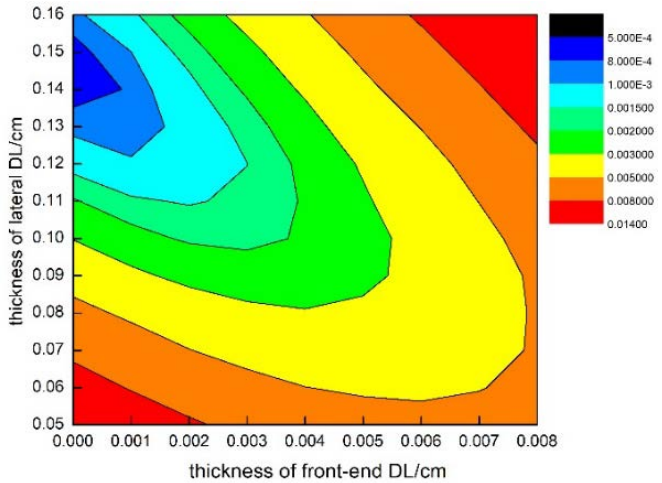

Fig. 7. *SSR* contour of low-energy and medium-energy gamma-ray efficiencies as thicknesses of front-end and lateral DLs varying.

The contour shows that the optimal DLs have a thicker lateral DL (ranges from 0.14 cm to 0.15 cm) and a very thin frontend DL (0.00001cm). Relative deviations of between measured efficiencies and calculated ones with the DLs mentioned above are listed in Table 2. These thicknesses of front-end and lateral DLs are both appropriate because the relative deviations are all within the uncertainties of the experiment results.

Table 2 Relative deviations of efficiencies between experiments and calculations

Energy/keV	Eff_{exp}	Thicknesses of the front-end/lateral DLs/cm	
		0.00001/0.14	0.00001/0.15
59.541	2.356E-02(2.1%)	-0.9%	-1.4%
80.586	2.301E-02(2.5%)	1.5%	1.0%
121.783	2.123E-02(2.4%)	1.6%	1.1%
160.613	1.889E-02(2.4%)	-1.2%	-1.8%

To pin the optimal thickness for the lateral DL, the backend DL is engaged and efficiencies of different gamma-ray regions are calculated. The contours (Fig. 8) are SSR of a) low-energy gamma-ray (<=160 keV), b) medium-energy gamma-ray (160 keV~1000 keV), and c) high-energy gamma-ray (>1000 keV) efficiencies as the lateral and back-end DLs change, respectively. The initial lateral and back-end DLs are set as 0.13 cm and 0.12 cm, respectively. The steps of the lateral and back-end DLs are set as 0.01 cm and 0.02 cm, respectively.

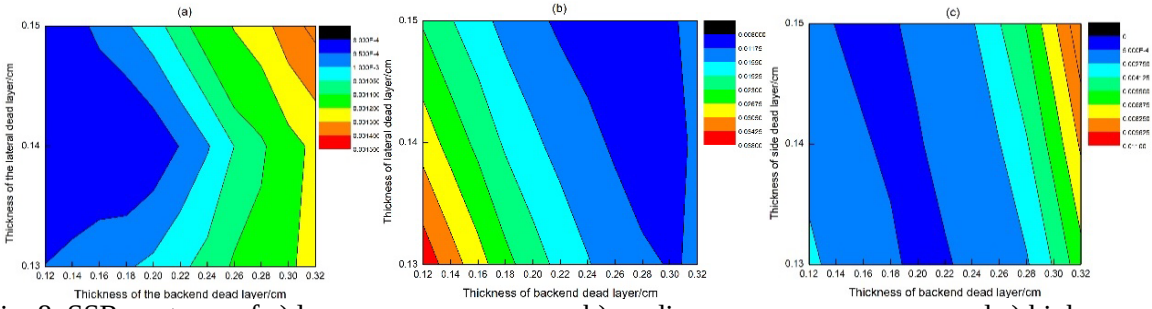

Fig. 8. SSR contours of a) low-energy gamma-ray, b) medium-energy gamma-ray and c) high-energy gamma-ray efficiencies as the lateral and backend DLs varying.

The low-lying overlap in SSR contours of low-energy (Fig. 8(a)) and high-energy (Fig. 8(c)) gamma-ray efficiencies locates at the lateral DL of 0.14 cm and the backend DL of 0.18 cm. While the optimal DLs for medium-energy gamma-ray efficiencies trend to be thicker (Fig. 8(b)). Relative deviations of gamma-ray efficiencies between experiments and calculations for the case of the lateral DL at 0.14 cm and the backend DL at 0.18 cm is illustrated in Fig. 6(b). It shows that points of calculated efficiencies are within 2% deviation compared with ones of the measurements for the low and high-energy rays, while most points of calculated efficiencies are beyond 4% than those of the measurements for medium-energy rays. It can be deduced that the lateral DL which affects the medium-energy gamma-ray efficiencies sensitively should be thicker than the current value.

However, increasing thickness for the whole lateral DL will decrease efficiencies for low-energy gamma rays. Since the optimal front-end DL is very thin (0.00001 cm) it is hard to be decreased again to fit a thicker lateral DL for the low-energy gamma rays.

To solve the problem, the lateral DL is modified to have a non-uniform thickness. Considering the locations of fastening belt and the screws, the vicinity electric field in the

crystal will be changed. The position of a new-added lateral DL is fixed at the same height of the fastening belt and is adjacent to the original lateral DL (Fig. 9). The thickness (*d*) and the width (*L*) of the new-added DL are optimized by the minimal SSR of the medium-energy gamma-ray efficiencies. The initial values of *d* and *L* are set as 0.02 cm and 0.2 cm, respectively. The steps of *d* and *L* are set as 0.02 cm and 0.2 cm, respectively. The SSRs of low-energy and high-energy gamma-ray efficiencies are also calculated. The SSR contours for different energy range of gamma-rays are shown in Figure 10.

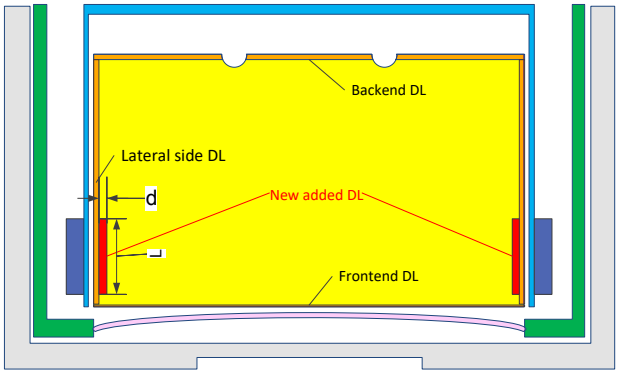

Fig. 9. Distribution of dead layers in the crystal.

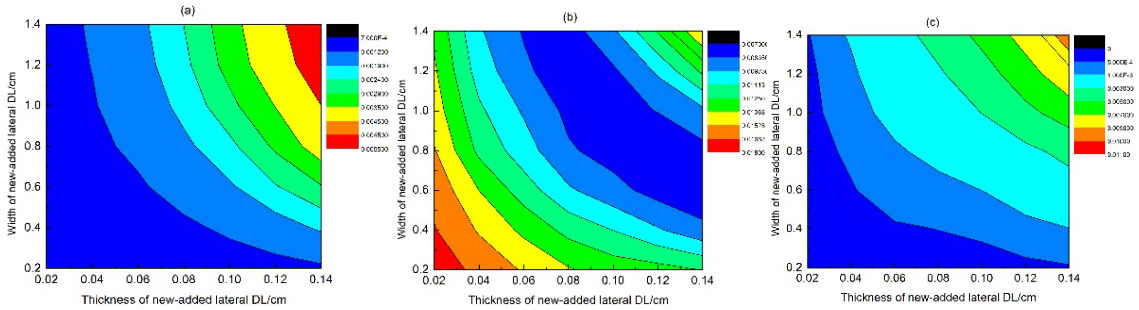

Fig. 10. SSR of a) low-energy gamma-ray, b) medium-energy gamma-ray and c) high-energy gamma-ray efficiencies as the thickness and the width of the new-added lateral DL varying.

The new-added lateral DL pined at *d* of 0.14 cm and *L* of 0.6 cm improves the minimal SSR of medium-energy gamma rays from less than 0.017(Fig.8(b)) to less than 0.00835 (Fig.10(b)). While this new-added DL increases the SSRs of low-energy and high-energy gamma rays. Relative deviations of efficiencies between calculations and experiments are shown in Fig. 6(c). The calculated efficiencies of MC model with corrected DLs are shown as green hollow circles in Fig. 1. Fig. 6(c) shows that almost all calculated efficiencies fall within 4% interval except one for 160 keV gamma ray. The reason of the exception may attribute to the weak SNR (signal to noise ratio) which is less than 0.18.

Compared with the MC model without any DLs (Fig. 6(a)), MC model with corrected DLs (Fig. 6(c)) improves the calculated efficiencies tremendously. Compared with the model with initial DLs (Fig. 6(b)), the model with corrected DLs eliminates offset of the calculated efficiencies, and makes the calculated efficiencies distribute equally around the measured ones within 4% interval.

3. Conclusion

A precise model of HPGe detector for efficiency calibration is constructed here. The geometric dimension and detailed subtle structures such as circinate groove on the rear end of the germanium crystal, the curving beryllium window, and the non-homocentric PMMA

bracket are accurately determined by X-ray radiography. DLs of the germanium crystal is determined by tracing the minimal SSR of gamma-ray efficiencies. Nonuniform distribution of the lateral DL is supposed and the corresponding model improves the accuracy of the calculated efficiencies.

Acknowledgement

Special thanks to Li Shigeng of Institute of Applied electronics, China Academy of Engineering Physics for the X-ray radiography and 3-D model reconstruction.

Funding. This work was supported by the National Natural Science Foundation of China (No. 11905198).

References

1. E. Moses, The national ignition facility (NIF) and the National Ignition Campaign (NIC), LLNL-CONF-417770[R], Lawrence Livermore National Laboratory, 2009.
2. Jiang Shaoen, Ding Yongkun, Liu Shenye, et al. Recent inertial confinement fusion experiments and diagnostic techniques on the Shenguang laser facility [J]. Physics, 2010, 39(08).
3. T.J. Murphy, C.W. Barnes, R.R. Berggren, et al. Nuclear diagnostics for the National Ignition Facility[J]. Review of Scientific Instruments, 2001, 72(1): 773-779.
4. J. Kilkenny. NIF Diagnostics: now and in the future, LLNL-PRES-558191[R]. Lawrence Livermore National Laboratory, 2012.
5. M.A. Stoyer, C.J. Cerjan, K.J. Moody, et al. Radiochemistry: A versatile diagnostic for the NIF ignition campaign, LLNL-TR-405043[R]. Lawrence Livermore Laboratory, 2008.
6. R.D. Hoffman, C.J. Cerjan, D.A. Shaughnessy, et al. Radiochemistry diagnostics for the National Ignition Facility, LLNL-PROC-426088[R]. Lawrence Livermore Laboratory, 2010.
7. M.A. Stoyer, C.A. Velsko, B.K. Spears, D.G. Hicks, G.B. Hudson et al. Collection of solid and gaseous samples to diagnose inertial confinement fusion implosions [J]. Rev. Sci. Instrum. 83, 023505 (2012)
8. G.P. Grim, P.A. Bradley, T.A. Bredeweg, et al. Prompt radiochemistry at the National Ignition Facility[J]. Review of Scientific Instruments, 2008, 79(10): 10E503.
9. J.M. Gostic, D.A. Shaughnessy, P.M. Grant, et al. Development of solid collection diagnostics on NIF through blast shield analysis, LLNL-PROC-520621[R], Lawrence Livermore National Laboratory, 2011.
10. Song Zifeng, Tang Qi, Chen Jiabin et al. DT neutron yield diagnosis by copper activation on Shenguang-III laser facility [J]. High Power Laser and Particle Beams, 2015, 27(11): 101-105.
11. Song Zifeng, Chen Jiabin, Liu Zhongjie, et al. Evaluation of uncertainty in DD neutron yield diagnosis by indium activation. High Power Laser and Particle Beams, 2014, 26(3): 120-125.
12. A.C. Hayes. Diagnosing Mix in NIF Capsules with Charged-particle Reactions and RIF Neutrons, LA-UR-08-5693[R]. Los Alamos National Laboratory, 2008.
13. D.A. Shaughnessy, C. Cerjan, K.J. Moody, L. Bernstein, R. Hoffman, et al. Evaluation of the Radiochemical diagnostic as an assessment of fuel-ablator mix and fuel ρR, LLNL-TR-472595[R], Lawrence Livermore National Laboratory, 2011.
14. R. Fortner, L. Bernstein, C. Cerjan, et al. Ignition Failure Mode Radiochemical Diagnostics Initial Assessment, UCRL-TR-230178[R]. Lawrence Livermore National Laboratory, 2007.

15. Charles Cerjan, Radiochemistry for NIF Implosion Diagnostics, CRL PRES-235692[R], NIF Workshop on Nuclear Astrophysics, 2007.
16. Azbouche, A., Belgaid, M., Mazrou, H., Monte Carlo calculations of the HPGe detector efficiency for radioactivity measurement of large volume environmental samples[J], Journal of Environmental Radioactivity, 2015, 146: 119-124.
17. Azli, Tarek, Chaoui, Zine-El-Abidine. Performance revaluation of a N-type coaxial HPGe detector with front edges crystal using MCNPX[J], Applied Radiation and Isotopes, 2015,97: 106-112.
18. Chuong, Huynh Dinh, Thanh, Tran Thien, Ngoc Trang, Le Thi, et al. Estimating thickness of the inner dead-layer of n-type HPGe detector [J], Applied Radiation and Isotopes, 2016, 116: 174-177.
19. Dryak, Pavel, Kovar, Petr, Experimental and MC determination of HPGe detector efficiency in the 40–2754 keV energy range for measuring point source geometry with the source-to-detector distance of 25cm [J], Applied Radiation and Isotopes, 2006, 64: 1346-1349.
20. Maidana, Nora L. Vanin, Vito R. García-Alvarez, Juan A. et al. Experimental HPGe coaxial detector response and efficiency compared to Monte Carlo simulations[J], Applied Radiation and Isotopes, 2016, 108: 64-74.
21. M.T. Haj-Heidari, M.J. Safari, H. Afarideh, H. Rouhi, Method for developing HPGe detector model in Monte Carlo simulation codes, Radiation Measurements, 2016, 88: 1-6.
22. J. Eberth, J. Simpson, From Ge(Li) detectors to gamma-ray tracking arrays–50 years of gamma spectroscopy with germanium detectors, Progress in Particle and Nuclear Physics, 2008, 60: 283-337.
23. X-5 Monte Carlo Team, “MCNP – A General N-Particle Transport Code, Version 5” https://laws.lanl.gov/vhosts/mcnp.lanl.gov/mcnp5.shtml.